# Effects of different population, orientation, and alignment relaxation rates in resonant four-wave mixing

Skip Williams[a)] and Larry A. Rahn[b)]
*Combustion Research Facility (MS 9051), Sandia National Laboratories, Livermore, California 94551*

Richard N. Zare[b)]
*Department of Chemistry, Stanford University, Stanford, California 94305*

We present a combined theoretical and experimental study on the effects of different population, orientation, and alignment relaxation rates in resonant four-wave mixing (RFWM). Signal generation in RFWM can be viewed as the formation of and scattering from laser-induced population, orientation, and alignment gratings. We show that the relative contributions from the upper-state and lower-state population, orientation, and alignment gratings to the observed output signal can be changed by varying the polarizations of the three input fields. A theory is developed to account for these changes in collisional environments where the three multipole moments of the total angular momentum distribution, i.e., the population, the orientation, and the alignment, relax unequally. This theory is applied to the OH radical in an atmospheric-pressure $H_2/O_2/He$ flame for which we have measured the line profiles using high-resolution degenerate and nearly degenerate four-wave mixing. We find that orientation and alignment gratings relax more rapidly than population gratings for low rotational levels of OH in the presence of He but at essentially the same rate for high rotational levels. A discussion is presented of the importance of this effect in the interpretation of RFWM experiments. © *1996 American Institute of Physics.* [S0021-9606(96)01410-6]

## I. INTRODUCTION

Laser-induced grating spectroscopy (LIGS) is a powerful tool for studying phenomena in all phases of matter.[1] Resonant four-wave mixing (RFWM) methods such as degenerate, nearly degenerate, and two-color four-wave mixing (DFWM, NDFWM, and TC-RFWM) are important special cases of LIGS and have been developed in both the frequency[2–8] and time[9–15] domains. One important application of RFWM is the study of reacting gaseous media, including plasma[16] and combustion[17] environments. Measurements of molecular temperature,[18–21] concentration,[22–24] and velocity distributions[25,26] have been demonstrated. In addition RFWM methods have been recently applied to double resonance spectroscopy of molecules[27] and to background-free stimulated emission pumping spectroscopy of stable[28] and transient species.[8,29] A common goal of the frequency-domain experiments is to interpret the relative intensity distribution of the diffracted light; however, RFWM requires an understanding of polarization, relaxation, and dephasing effects before relative internal-state distributions can be extracted from the signal intensities.

Theoretical[3–6,8,30–36] and experimental[8,21,33,37–41] efforts in this area have dealt with many of these effects. To our knowledge, however, the effect of elastic collisions which reorient the absorbing molecules, i.e., change the orientation and alignment, has not been determined. The aim of this paper is to demonstrate that elastic reorienting collisions can have a marked effect on the interpretation of RFWM spectra. This goal is accomplished by modeling frequency-domain DFWM and NDFWM data obtained for the OH radical in an atmospheric-pressure $H_2/O_2/He$ flame. The expressions presented have been derived via time-independent diagrammatic perturbation theory and therefore describe the DFWM and NDFWM polarization, collisional, and velocity effects in the weak-field, steady-state limit. The details of the derivation have been presented elsewhere.[6] This treatment makes explicit how the magnitude of the DFWM signal depends on the polarizations of the other three beams and the collisional relaxation caused by the environment.

The remainder of the paper is organized into five sections. In Sec. II, we present expressions for DFWM and NDFWM signal intensities as a function of input polarization, collisional relaxation and dephasing, and experimental geometry. In Sec. III we describe the experimental apparatus and conditions. In Sec. IV we present DFWM and NDFWM data of the OH radical in an atmospheric-pressure $H_2/O_2/He$ flame as a function of field polarization and discuss these results in Sec. V. In Sec. VI we present conclusions of our findings.

## II. THEORETICAL EXPRESSIONS

In four-wave mixing three incoming waves with electric fields $\mathbf{E}_1(\mathbf{r},t)$, $\mathbf{E}_2(\mathbf{r},t)$, and $\mathbf{E}_3(\mathbf{r},t)$, propagation vectors $\mathbf{k}_1$, $\mathbf{k}_2$, and $\mathbf{k}_3$, and frequencies $\omega_1$, $\omega_2$, and $\omega_3$ interact through the third-order nonlinear susceptibility $\chi^{(3)}$ to generate

---

[a)]Present address: Chemistry Science and Technology Division 4, Mail Stop J586, Los Alamos National Laboratory, Los Alamos, NM 87545.
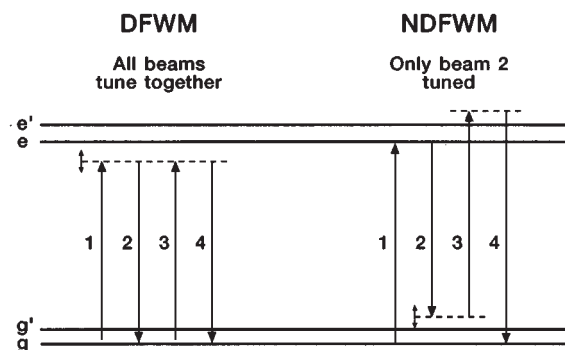[b)]Authors to whom correspondence should be addressed.

FIG. 1. Energy-level diagram for DFWM and NDFWM of a degenerate two-level system. In the figure we restrict the letters $g$ and $g'$ to refer to two degenerate magnetic sublevels (either the same or different) of the lower level (usually the ground electronic state), and the letters $e$ and $e'$ refer to two degenerate magnetic sublevels (either the same or different) of the upper level (usually another electronic state). These levels are assumed to be characterized by total angular momentum $\mathbf{J_g}$ and $\mathbf{J_e}$, respectively.

a fourth field, $\mathbf{E}_4$, with propagation vector $\mathbf{k}_4$ and frequency $\omega_4$. The electric fields are defined as

$$\mathbf{E_j}(\mathbf{r},t)=\tfrac{1}{2}\mathbf{E}_j e^{-i(\omega_j t-\mathbf{k_j}\cdot\mathbf{r})}+\text{c.c.};\quad \mathbf{E_j}=E_j\boldsymbol{\epsilon}_j, \quad (1)$$

where $\mathbf{E_j}$ is the vector amplitude, $E_j$ is the scalar amplitude, and $\boldsymbol{\epsilon}_j$ is the normalized ($\boldsymbol{\epsilon}_j\cdot\boldsymbol{\epsilon}_j^*=1$) polarization unit vector of the electric field labeled $j$. The conventions for expressing the unit vectors are given in the Appendix of Ref. 6.

For fully resonant DFWM and NDFWM we assume that the excitation bandwidth is sufficiently narrow compared with the density of states (including Doppler broadening) of the absorbing molecules so that the interaction is exclusively between the degenerate magnetic sublevels of the two levels involved in the one-photon resonant transition. These levels are characterized by total angular momentum quantum numbers $J_g$ and $J_e$ respectively. See Fig. 1. Describing the resulting coherence between these levels in terms of the total angular momentum distribution is convenient. The most complete description of the angular momentum distribution is in terms of state multipoles that represent the populations of the levels and the coherences existing between them.[42] The state multipoles are spherical tensors of rank $K$ and component $Q$ ($-K\leq Q\leq K$). The $Q=0$ components describe the projection of $\mathbf{J}$ onto the space-fixed $Z$ axis, and the $Q\neq0$ components describe the projection of $\mathbf{J}$ onto the space-fixed $XY$ plane. Here the monopole term ($K=0$) is proportional to the population. All odd rank multipoles (dipole, octopole, etc.) describe the orientation of the angular momentum, and all even rank multipoles (quadrupole, hexadecapole, etc.) are related to the alignment of the angular momentum.[43] We showed in a previous paper[6] that the highest allowed value of $K$ for unsaturated DFWM is 2. Therefore, we take the $K=0$, 1, and 2 terms to describe the (scalar) population, (dipolar) orientation, and (quadupolar) alignment, respectively.

We consider three input fields of arbitrary polarization that interact with an isotropic sample to produce a fourth field and assume that field propagation effects can be ignored
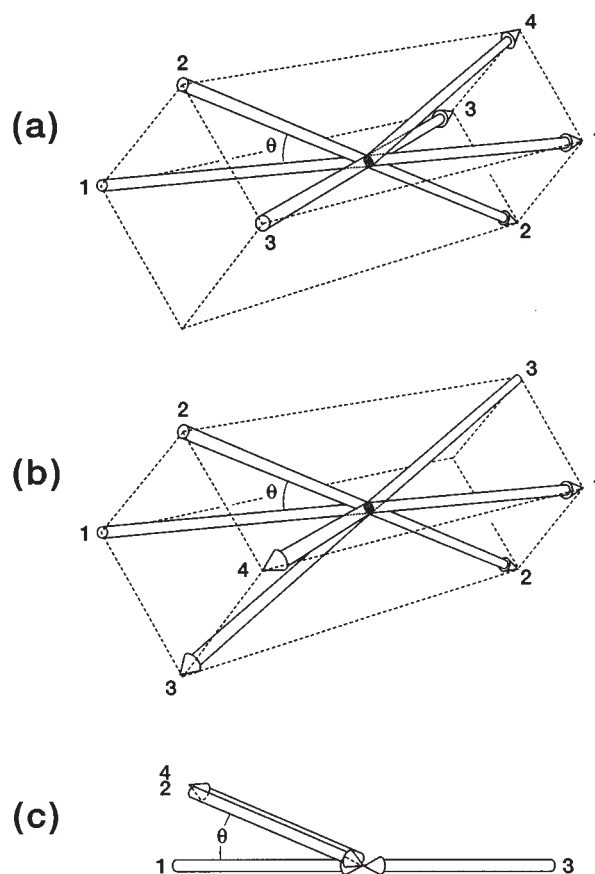


FIG. 2. Phase matching geometries: (a) Forward box, FB-DFWM; (b) Backward box, BB-DFWM; (c) Phase conjugate, PC-DFWM. The angle $\theta$ in the figure is typically less than 2°.

(negligible absorption). In our treatment, we assume that the RFWM process couples levels of sharp (definite) angular momentum $\mathbf{J}$ (omitting nuclear spin). Therefore, our treatment is general in that it applies to molecular species for which $J$ is a good quantum number. The general result is specialized to apply to linearly polarized fields that interact in nearly collinear phase-matching geometries in collisional environments where the multipole moments of the total angular momentum distribution relax independently (isotropic relaxation). Figure 2 shows the three DFWM and NDFWM phase-matching geometries discussed in this paper.

The significant contributions to the DFWM and NDFWM signal intensities are derived using diagrammatic perturbation theory[2,44,45] and are evaluated using a spherical tensor formalism.[46,47] Sixteen diagrams are necessary to account for all of the time orderings of the input fields that correspond to the resonant energy-level diagrams of Fig. 1. We express the signal intensities in terms of multipole components, because it provides a well-developed and efficient way of using the inherent symmetry of the system and enables dynamic and geometric factors to be separated from each other. This treatment yields the following expression[6] for the DFWM and NDFWM signal intensities in the perturbative (weak-field) limit:

$$I_{\text{DFWM}} \propto \left[ N_g - \frac{(2J_g+1)}{(2J_e+1)} N_e \right]^2 [B_{ge}(J_g,J_e)]^4 I_1 I_2 I_3 \left| \sum_{K=0}^{2} \{ L_{12}^g(\delta,\Delta,K) G(J_g,J_e;K) F(\boldsymbol{\epsilon}_4,\boldsymbol{\epsilon}_1,\boldsymbol{\epsilon}_3,\boldsymbol{\epsilon}_2;K) \right.$$

$$+ L_{12}^e(\delta,\Delta,K) G(J_e,J_g;K) F(\boldsymbol{\epsilon}_4,\boldsymbol{\epsilon}_1,\boldsymbol{\epsilon}_3,\boldsymbol{\epsilon}_2;K) + L_{32}^g(\delta,\Delta,K) G(J_g,J_e;K) F(\boldsymbol{\epsilon}_4,\boldsymbol{\epsilon}_3,\boldsymbol{\epsilon}_1,\boldsymbol{\epsilon}_2;K)$$

$$\left. + L_{32}^e(\delta,\Delta,K) G(J_e,J_g;K) F(\boldsymbol{\epsilon}_4,\boldsymbol{\epsilon}_3,\boldsymbol{\epsilon}_1,\boldsymbol{\epsilon}_2;K) \} \right|^2, \tag{2}$$

where

$$G(J,J';K) = (2J_g+1) \begin{Bmatrix} J & J & K \\ 1 & 1 & J' \end{Bmatrix}^2, \tag{3}$$

$$F(\boldsymbol{\epsilon}_4,\boldsymbol{\epsilon}_i,\boldsymbol{\epsilon}_j,\boldsymbol{\epsilon}_2;K) = \sum_{Q=-K}^{K} (-1)^Q [\epsilon_4^{*(1)} \otimes \epsilon_j^{(1)}]_Q^{(K)} [\epsilon_2^{*(1)} \otimes \epsilon_i^{(1)}]_{-Q}^{(K)}, \tag{4}$$

and

$$L_{j2}^n(\delta,\Delta,K) = \int \frac{f(\mathbf{v}) d^3\mathbf{v}}{[\delta - (\mathbf{k_j} - \mathbf{k_2}) \cdot \mathbf{v} + i\Gamma_n(K)][\Delta - \delta + \mathbf{k_4} \cdot \mathbf{v} - i\Gamma_{eg}]} \left\{ \frac{1}{[\Delta + \delta + \mathbf{k_2} \cdot \mathbf{v} + i\Gamma_{eg}]} - \frac{1}{[\Delta + \mathbf{k_j} \cdot \mathbf{v} - i\Gamma_{eg}]} \right\}. \tag{5}$$

In Eq. (2), $N_g$ and $N_e$ are the total populations of the levels $g$ and $e$, respectively, in the absence of applied fields, $B_{ge}(J_g,J_e)$ is the Einstein absorption coefficient that connects the level with total angular momentum $\mathbf{J}_g$ to the level with $\mathbf{J}_e$, $I_j$ is the intensity of the electric field labeled $j$, and the $K=0$, 1 and 2 terms describe the contributions from the (scalar) population, (dipolar) orientation, and (quadupolar) alignment, respectively. In Eq. (3) the $G(J,J';K)$ factors are simply $6-j$ symbols and depend only on $K$, $J_g$, and $J_e$, i.e., the type of spectroscopic transition probed ($P$, $Q$, or $R$ branch). Conversely, the $F(\boldsymbol{\epsilon}_4,\boldsymbol{\epsilon}_i,\boldsymbol{\epsilon}_j,\boldsymbol{\epsilon}_2;K)$ factors of Eq. (4) depend on the field polarizations denoted by $\boldsymbol{\epsilon}_j$ but not on $J_g$ and $J_e$. The $G(J,J';K)$ and $F(\boldsymbol{\epsilon}_4,\boldsymbol{\epsilon}_i,\boldsymbol{\epsilon}_j,\boldsymbol{\epsilon}_2;K)$ factors are given in Tables IV and V, respectively, of Ref. 6.

In Eq. (5) the $L_{j2}^n(\delta,\Delta,K)$ are complex line shape functions and $f(\mathbf{v})$ is the normalized (Maxwell–Boltzmann) velocity-distribution function, $\Delta = \omega_0 - \omega_1 = \omega_0 - \omega_3$ is the spectral detuning of $\mathbf{E}_1$ and $\mathbf{E}_3$ from $\omega_0$ where $\hbar\omega_0$ is the energy difference between the $e$ and $g$ levels $\delta = \omega_1 - \omega_2 = \omega_3 - \omega_2$ is the spectral detuning of $\mathbf{E}_2$ from $\mathbf{E}_1$ and $\mathbf{E}_3$, $\mathbf{k}_j$ is the propagation vector of the field label $j$, $\mathbf{v}$ is the velocity vector of the absorbing molecule, and $2\Gamma_{eg}$ is the homogeneous (no Doppler broadening) full-width-at-half-maximum (FWHM) of a dipolar transition between the $e$ and $g$ levels. The sub- and superscripts on $L$ refer to the first terms of Eq. (5). Specifically for the line shape function $L_{j2}^n(\delta,\Delta,K)$, $n$ is the quantum-state label of $\Gamma_n(K)$, and $j$ is the field label, either 1 or 3, that corresponds to the $\mathbf{k}$-vector difference $\Delta\mathbf{k_{j2}} = (\mathbf{k_j} - \mathbf{k_2})$. The $\Gamma_n(K)$ are defined as follows: $\Gamma_n(0)$ is the relaxation rate of the global population of the $n$th level, and $\Gamma_n(K=1)$ and $\Gamma_n(K=2)$ are the relaxation rates of the molecular orientation and alignment of the $n$th level, respectively.

Effects resulting from finite laser bandwidths and velocity changing collisions are not included in Eq. (5), and to our knowledge, have not been treated. Furthermore, only colli-

sional relaxation is considered (no spontaneous emission), and as written, the specific collisional rates are dependent on temperature but independent of velocity. The velocity integration of Eq. (5) has been performed by many authors[2–4,30,48,49] and is not discussed here. Note that in a DFWM experiment $\delta=0$ and $\Delta$ is varied, and conversely, in *these* NDFWM experiments $\Delta=0$ and $\delta$ is varied.

Equation (2) represents a general solution to the DFWM and NDFWM signal intensities for molecular systems (no hyperfine structure) excited by electric dipole radiation in the weak-field, steady-state limit and can be evaluated explicitly for the phase-matching geometry and polarization configuration of interest. Physically, the DFWM signal intensity of Eq. (2) is interpreted as resulting from the contributions of four terms: the first term represents the contribution of the diffraction of wave 3 from a ground-state grating formed by fields 1 and 2; the second term represents the contribution of the diffraction of wave 3 from an excited-state grating formed by fields 1 and 2; the third term represents the contribution of the diffraction of wave 1 from a ground-state grating formed by fields 3 and 2; and the fourth term represents the contribution of the diffraction of wave 1 from an excited-state grating formed by fields 3 and 2. In addition, the multipole components can be interpreted as ground- and excited-state population, orientation, alignment gratings for $K=0$, 1, and 2, respectively. This treatment demonstrates that DFWM and NDFWM signals may be regarded as arising from the contributions of twelve different gratings! The gratings can be distinguished by spacing ($\Delta\mathbf{k}_{12}$ or $\Delta\mathbf{k}_{32}$), by the level in which the grating is formed (ground or excited), and by the multipole nature of the grating (population, orientation, or alignment).

## III. EXPERIMENTAL DETAILS

In the DFWM experiments $\mathbf{E}_1$, $\mathbf{E}_2$, and $\mathbf{E}_3$ are supplied from a cw ring-dye laser that is pulse amplified by a single-

mode Nd:YAG laser. The laser output is frequency doubled in $KD^*P$ to produce laser beams at $\sim 308$ nm having pulse widths of $\sim 20$ ns (FWHM) and bandwidths of $\sim 0.001$ cm$^{-1}$ (FWHM). In the experiment the laser frequency is scanned across selected $^RQ_{21}$-branch transitions of the OH $A\ ^2\Sigma^+ - X\ ^2\Pi (0,0)$ band.[50,51] Note transitions are designated by $^{\Delta N}\Delta J_{F'}F''(J'')$ where the single prime refers to the upper state, the double prime refers to the lower state, and $F$ is $F_1$ or $F_2$. In the NDFWM experiments $\mathbf{E}_1$ and $\mathbf{E}_3$ are supplied from the same high-resolution, pulse-amplified laser system, and field $\mathbf{E}_2$ is produced from a separately tunable, but otherwise similar, pulse-amplified laser system. In the experiment $\mathbf{E}_2$ is spectrally detuned from $\mathbf{E}_1$ and $\mathbf{E}_3$ which are maintained at the line center of selected $^RQ_{21}$-branch transitions of the OH $A\ ^2\Sigma^+ - X\ ^2\Pi (0,0)$ band. In all of the experiments the fields are overlapped in time. Each field is linearly polarized, collimated, and apertured to produce a Gaussian beam profile with diameter of 1 mm (FWHM). Weak field intensities are used in these experiments to avoid saturation effects. Typical field intensities used here are 10 kW/cm$^2$ which are more than 50 times smaller than the calculated saturation intensities.[21,52] All signals are detected with a photomultiplier, digitized, normalized to the input field intensities, averaged over 30–60 laser shots, and stored on a computer for further analysis. Unless otherwise stated, the reported errors include statistical and experimental uncertainties and represent $1\sigma$ deviations.

The experiment is configured so that any linear polarization configuration is obtained by rotating half-wave plates. After polarization rotation each beam is directed by one additional mirror. This configuration maintains the polarization purity ($>96\%$) and minimizes energy loses caused by differences in reflection of $S$- and $P$-polarized light. In what follows $X$ and $Y$ denote orthogonal linear polarization states. In addition we use the notation previously established a polarization configuration is given as $\epsilon_4\epsilon_1\epsilon_3\epsilon_2$ where $\epsilon_j$ is the polarization vector of the electric field labeled $j$. For example the $YYXX$ polarization configuration corresponds to $\mathbf{E}_4$ and $\mathbf{E}_1$ being $Y$ polarized and $\mathbf{E}_3$ and $\mathbf{E}_2$ being $X$ polarized.

All measurements are made in the post-flame gases of a $H_2/O_2/He$ flat-flame burner using gas flows of 4.8 slm (standard liters per minute) $H_2$, 3.0 slm $O_2$, and 14.5 slm of He. This results in an equivalence ratio of 0.8 (excess oxygen). Measurements are made at a height of $5.5\pm0.5$ mm above the burner which corresponds to a temperature of $1380\pm70$ K as measured with a radiation-corrected thermocouple. At this height the combustion reaction is complete[53] and the post-flame gas composition is calculated to be 3% $O_2$, 24% $H_2O$ and 73% He. For the $^RQ_{21}$-branch transitions studied here linear absorption of the beams in this flame amounted to less than 2%.

## IV. RESULTS

### A. DFWM line profiles

The backward box DFWM (BB-DFWM) configuration is employed here because this nonplanar configuration maintains the sub-Doppler spectral resolution of phase conjugate
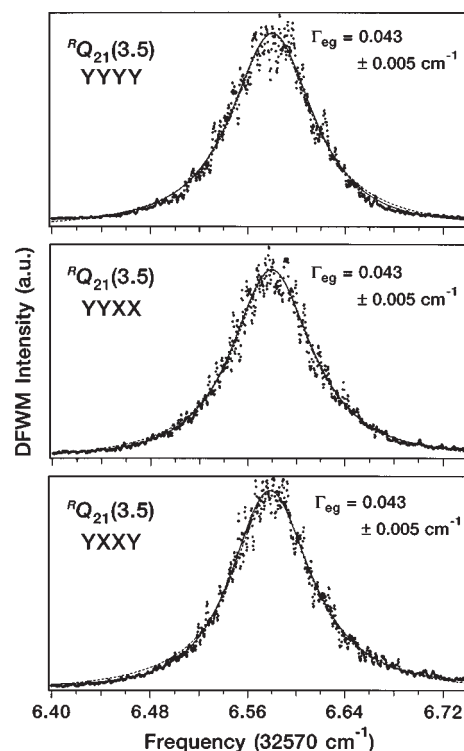


FIG. 3. BB-DFWM line profiles of the $^RQ_{21}(3.5)$ transition of the OH $A\ ^2\Sigma^+ - X\ ^2\Pi\ (0,0)$ band as a function of polarization. In the figure $X$ and $Y$ denote orthogonal linear polarization states, and the polarizations of the fields are given in the order $\epsilon_4\epsilon_1\epsilon_3\epsilon_2$. The solid curves are fits of the data to Eq. (2) and the dashed curves are fits of the data to Eq. (6).

DFWM (PC-DFWM) but offers superior signal-to-noise ratios resulting from better scattered light discrimination. Figure 3 shows BB-DFWM line profiles of the $^RQ_{21}(3.5)$ transition of the OH $A\ ^2\Sigma^+ - X\ ^2\Pi(0,0)$ band as a function of input field polarization. The solid curves are nonlinear least-squares fits of the data to Eq. (2), and the dashed curves are fits of the data to a Lorentzian line shape. In what follows all the modeled line shapes assume a Maxwell–Boltzmann velocity distribution corresponding to a temperature of 1380 K. Because $2\Gamma_{eg}/\Delta\omega_D = 0.41$ for the $H_2/O_2/He$ flame studied here, where $\Delta\omega_D$ is the Doppler full-width, the model line shape is expected to be nearly Lorentzian and insensitive to the ground and excited state relaxation rates, $\Gamma_g$ and $\Gamma_e$, respectively. This behavior is discussed in more detail in Sec. V A. Both expectations are indeed met as can been seen by the quality of the simple Lorentzian fits to the data. Therefore as a result of the insensitivity of the model line shape to $\Gamma_g$ and $\Gamma_e$, we set $\Gamma_{eg}=\Gamma_g=\Gamma_e$ and varied the homogeneous broadening parameter $\Gamma_{eg}$ for best fits.

As can be seen in the figure, the line profile is the same in shape and width for each polarization configuration. Fitting twelve $^RQ_{21}(3.5)$ line profiles (four of each polarization configuration) to Eq. (2) yields an average value of 0.043 $\pm0.005$ cm$^{-1}$ for $\Gamma_{eg}$. We obtained similar results for the $^RQ_{21}(1.5)$ and $^RQ_{21}(8.5)$ transitions, i.e., nearly Lorentzian line profiles with polarization-independent line widths. The average homogeneous dephasing rates of the $^RQ_{21}(1.5)$ and

TABLE I. Fitted relaxation and dephasing rates[a] for OH in an $H_2/O_2/He$ flame at 1380 K as a function of $^RQ_{21}$-branch transition of the $A\ ^2\Sigma^+ - X\ ^2\Pi$ (0,0) band.

| Transition | $\Gamma_{eg}$ | $\Gamma_n(K=0)$ | $\Gamma_n(K>0)$ |
|---|---|---|---|
| $^RQ_{21}(1.5)$ | 0.047 | 0.020 | 0.039 |
| $^RQ_{21}(3.5)$ | 0.043 | 0.025 | 0.035 |
| $^RQ_{21}(8.5)$ | 0.038 | 0.019 | 0.019 |

[a]The error of each entry is $\pm 0.005$ and all values are in units of $cm^{-1}$.

$^RQ_{21}(8.5)$ transitions obtained by fitting the several line profiles to Eq. (2) are $0.047 \pm 0.005$ $cm^{-1}$ and $0.038 \pm 0.005$ $cm^{-1}$, respectively. See Table I.

## B. NDFWM line profiles

In the NDFWM experiments we chose the forward box configuration (FB-NDFWM), because it minimizes beam steering effects while maintaining sub-Doppler spectral resolution. Note that FB-DFWM does not offer sub-Doppler spectral resolution, because $\Delta$ is varied instead of $\delta$ in Eq. (5). In addition, the $YXYX$ and $YYXX$ polarization configurations are equivalent for this totally symmetric phase-matching geometry. Figure 4 shows FB-NDFWM line profiles of the $^RQ_{21}(1.5)$ transition of the OH $A\ ^2\Sigma^+ - X\ ^2\Pi$(0,0) band as a function of input field polarization. In Fig. 4 we see that the $YXXY$ spectrum is noticeably
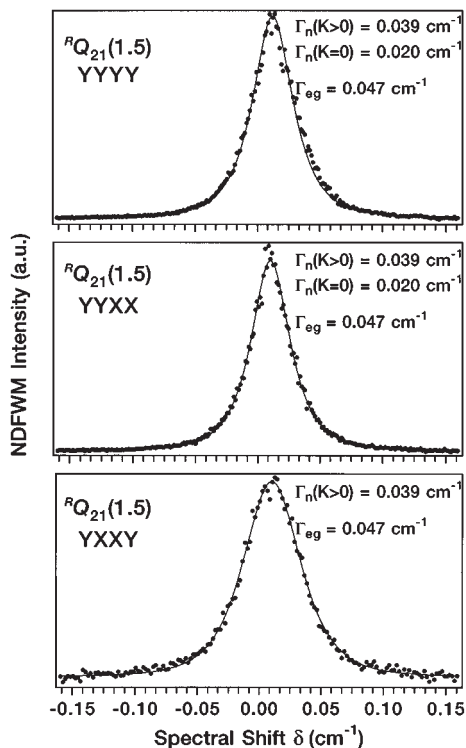


FIG. 4. FB-NDFWM line profiles of the $^RQ_{21}(1.5)$ transition of the OH $A\ ^2\Sigma^+ - X\ ^2\Pi$ (0,0) band as a function of polarization. In the figure $X$ and $Y$ denote orthogonal linear polarization states, and the polarizations of the fields are given in the order $\epsilon_4\epsilon_1\epsilon_3\epsilon_2$. The solid curves are theoretical fits of the data to Eq. (2).

broader than the $YYYY$ and $YYXX$ line profiles. Evaluating Eq. (2) for the $^RQ_{21}(1.5)$ transition shows that the $YXXY$ polarization configuration has no contribution from population gratings whereas the $YYYY$ and $YYXX$ polarization configurations have large contributions from population gratings. Specifically 61% and 74% of the total FB-NDFWM scattering *amplitude* results from population gratings for the $YYYY$ and $YYXX$ polarization configurations, respectively, (see Ref. 6, Figs. 5–7).

The solid curves in Fig. 4 are fits of the data to Eq. (2) assuming a minimal model for the collisional relaxation of OH. The minimal model is based on two main assumptions. First we assume that the orientation and the alignment relaxation rates of the $n$th level are the same and hence represent a Zeeman relaxation rate denoted as $\Gamma_n(K>0)$. This rate is distinguished from the population relaxation rate of the $n$th level denoted as $\Gamma_n(K=0)$. Second we assume that the collisional relaxation rates of the ground and excited states are the same, i.e., $\Gamma_g(K>0)=\Gamma_e(K>0)=\Gamma_n(K>0)$ and $\Gamma_g(K=0)=\Gamma_e(K=0)=\Gamma_n(K=0)$. Therefore, according to this minimal model, the DFWM and NDFWM signal responses are characterized by three fundamental relaxation rates namely, $\Gamma_{eg}$, $\Gamma_n(K=0)$, and $\Gamma_n(K>0)$.

The analysis of the FB-NDFWM line profiles is conducted as follows. BB-DFWM line profiles such as these shown in Fig. 3 are used to obtain $\Gamma_{eg}$. Then $YXXY$ FB-NDFWM line profiles are fit to Eq. (2) holding $\Gamma_{eg}$ fixed to obtain $\Gamma_n(K>0)$. Next $YYXX$ FB-NDFWM line profiles which, contrary to first impressions, have the largest population contributions are fit to Eq. (2) by holding $\Gamma_{eg}$ and $\Gamma_n(K>0)$ fixed to obtain $\Gamma_n(K=0)$. As a final self-consistency check, $YYYY$ FB-NDFWM line profiles are generated using all of the previously obtained fit values and compared with the experimental data. The data shown in Fig. 4 are in good agreement with the predictions of Eq. (2) and the significant differences among the relaxation rates demonstrate that at least three rates (minimal model) are necessary to account for the observed line profiles. If the $YYYY$ FB-NDFWM line profiles are free fitted the chi squared values of the fits decrease by only 13%. Note that the Zeeman relaxation rate is approximately twice the population relaxation rate for the $^RQ_{21}(1.5)$ transition, i.e., $\Gamma_n(K>0)/\Gamma_n(K=0)=2.0$. Good quality fits are also obtained for the $^RQ_{21}(3.5)$ and $^RQ_{21}(8.5)$ transitions although these transitions yielded $\Gamma_n(K>0)/\Gamma_n(K=0)$ ratios of 1.4 and 1.0, respectively. The Zeeman relaxation rate approaches the population relaxation rate as the total angular momentum of the levels involved in the transition is increased. The results of all the fits are shown in Table I.

## V. DISCUSSION

### A. Polarization ratios

DFWM has been extensively applied to the analysis of high-temperature gases such as flames and plasmas. These environments are typically characterized by large Doppler broadening (Doppler full-width equal to $\Delta\omega_D$). For these en-

TABLE II. BB-DFWM polarization ratios for the OH $A\,^2\Sigma^+ - X\,^2\Pi$ (0,0) band as a function of $^RQ_{21}$-branch transition.

| Transition | $P\left(\dfrac{\epsilon_4\epsilon_1\epsilon_3\epsilon_2}{YYYY}\right)$ | Theory $\Gamma(K)$ equal | BB-DFWM data H$_2$/O$_2$/He | Theory $\Gamma(K)$ unequal |
|---|---|---|---|---|
| $^RQ_{21}(1.5)$ | $YXYX$ | 0.172 | 0.301±0.114 | 0.396±0.050 |
| $^RQ_{21}(1.5)$ | $YYXX$ | 0.172 | 0.116±0.040 | 0.069±0.009 |
| $^RQ_{21}(1.5)$ | $YXXY$ | 0.029 | 0.012±0.004 | 0.012±0.002 |
| $^RQ_{21}(3.5)$ | $YXYX$ | 0.124 | 0.289±0.141 | 0.222±0.030 |
| $^RQ_{21}(3.5)$ | $YYXX$ | 0.124 | 0.079±0.040 | 0.082±0.010 |
| $^RQ_{21}(3.5)$ | $YXXY$ | 0.088 | 0.062±0.031 | 0.059±0.007 |
| $^RQ_{21}(8.5)$ | $YXYX$ | 0.113 | 0.179±0.076 | 0.113±0.014 |
| $^RQ_{21}(8.5)$ | $YYXX$ | 0.113 | 0.140±0.030 | 0.113±0.014 |
| $^RQ_{21}(8.5)$ | $YXXY$ | 0.107 | 0.138±0.018 | 0.107±0.013 |

vironments it is often the case that $\Delta\omega_D \gg 2\Gamma_{eg}$, and Eq. (2) takes on a very simple form[3,54] for PC- and BB-DFWM, namely,

$$
I_{\text{DFWM}} \propto \left[N_g - \frac{(2J_g+1)}{(2J_e+1)}N_e\right]^2 [B_{ge}(J_g,J_e)]^4 I_1 I_2 I_3
$$

$$
\times \left| L(\Delta)\sum_{K=0}^{2}\frac{G(J_g,J_e;K)F(\epsilon_4,\epsilon_1,\epsilon_3,\epsilon_2;K)}{\Gamma_g(K)} \right.
$$

$$
\left. + \frac{G(J_e,J_g;K)F(\epsilon_4,\epsilon_1,\epsilon_3,\epsilon_2;K)}{\Gamma_e(K)} \right|^2 , \tag{6}
$$

where

$$
L(\Delta) = \frac{\sqrt{\pi}}{ku}\frac{1}{(\Delta - i\Gamma_{eg})} . \tag{7}
$$

In Eq. (7) $k$ is the magnitude of the propagation vectors of the DFWM fields and $u$ is the most probable speed of the Maxwell–Boltzmann velocity distribution. Equations (6) and (7) define a simple Lorentzian line profile with a full-width-at-half-maximum of $2\Gamma_{eg}$, i.e., the line width is completely determined by the dipolar dephasing rate $\Gamma_{eg}$.

Since the BB-DFWM line widths in the limit of large Doppler broadening are independent of polarization it might be expected that the signal intensity as a function of polarization depends solely on the polarizations of the excitation fields. In Sec. II, however, we showed that the DFWM signal intensity results from the contributions of many types of gratings whose relaxation rates, and hence scattering efficiencies, can differ. Equation (6) shows this dependence, i.e., the absolute signal intensity depends on $\Gamma_{eg}$ and on the specific values of the population, the orientation, and the alignment relaxation rates of both the ground and excited state levels. Therefore to extract relative internal-state distributions from DFWM signals, a summation of the $G(J,J';K)$ and $F(\epsilon_4,\epsilon_i,\epsilon_j,\epsilon_2;K)$ factors weighted by the appropriate relaxation rates needs to be performed.

Table II shows polarization ratios for selected $^RQ_{21}$-branch transitions. The polarization ratios of Table II are defined as

$$
P\left(\frac{\epsilon_4\epsilon_1\epsilon_3\epsilon_2}{YYYY}\right) = \frac{I'_{\text{DFWM}}}{I_{\text{DFWM}}} , \tag{8}
$$

and are merely the ratio of the DFWM signal intensity for two different polarization configurations in which all other aspects of the experiment are the same. The experimental polarization ratios are obtained by setting the laser frequency at the line center of the $^RQ_{21}$-branch transitions and measuring the BB-DFWM signal intensity as the polarizations of the excitation fields are varied with half-wave plates.

The column labeled $\Gamma_n(K)$ equal theory of Table II is calculated assuming that population, orientation, and alignment gratings relax at the same rate. With this assumption the polarization ratios for $Q$-branch transitions are independent of differences in the excited- and ground-state relaxation rates.[6] A comparison of the predictions of this model with the experimental data shows that the $YXYX/YYYY$ polarization ratios are much larger than predicted whereas both the $YYXX/YYYY$ and $YXXY/YYYY$ polarization ratios are much smaller than predicted. Evaluating Eq. (2) shows that the both the $YYYY$ and $YXYX$ polarization configurations are dominated by population contributions whereas the $YYXX$ and $YXXY$ polarization configurations are dominated by orientation and alignment contributions. Therefore the BB-DFWM polarization ratio data suggest that OH population gratings relax more slowly than orientation and alignment gratings in this flame. This suggestion is verified by the different relaxation rates reported in Table I obtained from the NDFWM line shapes.

The fitted values of the relaxation rates of Table I are used to calculate the relaxation-rate-weighted BB-DFWM polarization ratios of Table II. Because the line profiles shown in Fig. 3 are nearly Lorentzian and well characterized by a single dephasing rate, Eq. (6) is used for this calculation.[55] The results of the calculation are given in the last column of Table II. The error in the theoretical calculations arises from the error in determining the relaxation rates which is $\pm 0.005$ cm$^{-1}$ for all. In Table II the $\Gamma_n(K)$ equal and the $\Gamma_n(K)$ unequal theories make very different predictions for the polarization ratios of the $^RQ_{21}(1.5)$ and $^RQ_{21}(3.5)$ transitions but predict the same values for the $^RQ_{21}(8.5)$ transition. The two theories are equivalent for the $^RQ_{21}(8.5)$ transition because the FB-NDFWM line profiles showed that the Zeeman and population relaxation rates are equal. The $\Gamma_n(K)$ equal theory predictions are outside the large error bars for the $^RQ_{21}(1.5)$ and $^RQ_{21}(3.5)$ transitions. The agreement with the $\Gamma_n(K)$ unequal theory is much improved and the trends in the data are reproduced.

Contributions from other types of intensity gratings, such as thermal[36,39–41] and electrostrictive,[36,56] can produce similar trends in DFWM polarization ratio data.[39] The trends in the polarization ratio data here, however, cannot be attributed to these types of intensity gratings, because the signal responses of these gratings were determined to be much smaller than the RFWM response in this flame.[40] Therefore the DFWM polarization ratio data further support the fact that at least three rates are necessary to interpret BB-DFWM signal intensities for low-$J$ values. The inclusion of more

rates, such as allowing for differences in the ground and excited state rates or in the orientation and alignment rates, would increase the accuracy of the calculation, but all these rates cannot be determined in a self consistent way from DFWM and NDFWM data alone.

## B. Relaxation and dephasing rates

In our analysis we define the excited state population relaxation rate as $\Gamma_e(K=0)=R+Q+A_{eg}$, where $R$, $Q$, and $A_{eg}$ are the rotational energy transfer (RET) rate, the quenching rate, and the Einstein spontaneous emission coefficient, respectively, for a specific rotational level of the $A\,^2\Sigma^+(\nu'=0)$ state. Furthermore we take the total RET rate for a specific rotational level to be the same for $X\,^2\Pi(\nu''=0,N''=N)$ and $A\,^2\Sigma^+(\nu'=0,N'=N)$ levels. Some experimental evidence supports this assumption.[57] This assumption allows us to define the ground state population relaxation rate as $\Gamma_g(K=0)=R$. In the atmospheric-pressure flame studied here, $A_{eg}$ is negligible compared to $R$ and $Q$, and $R$ is approximately six times larger than $Q$ (see below). Therefore our assumption that $\Gamma_g\approx\Gamma_e$ is justified. In what follows all rates are calculated as described in Sec. II C of reference 21 for our flame composition (3% $O_2$, 24% $H_2O$, and 73% He) and temperature (1380 K).

Lee, Kienle, and Kohse-Höinghaus (LKK)[58] studied energy transfer rates for OH in a low-pressure $H_2/O_2$/He flame at 1330 K and reported total RET rates and cross sections for specific rotational levels in the OH $A\,^2\Sigma^+(\nu'=0)$ state. The flame composition for their experimental conditions was calculated to be 26.3% $H_2O$, 0.8% OH, 5.1% $H_2$, 3.4%$O_2$, 9.3% H, 1.3% O, and 53.8% He. LKK determined that only two species, $H_2O$ and He, contributed significantly to the measured RET rates under these conditions. The RET contribution of He was estimated using calculated state-to-state He rate coefficients[59] and was subtracted from the total RET rate to give the $H_2O$ contribution. The following RET cross sections for the $F_2(N'=2)$, $F_2(N'=4)$, and $F_2(N'=9)$ levels at 1380 K are estimated from the tables and figures of Refs. 58 and 59: $142\pm50$ Å$^2$, $151\pm16$ Å$^2$, and $127\pm23$ Å$^2$ for $H_2O$; and $13.2\pm1.3$ Å$^2$, $8.5\pm0.8$ Å$^2$, and $1.7\pm0.2$ Å$^2$ for He.

Paul[60] has recently presented a model for the temperature-dependent quenching of OH $A\,^2\Sigma^+$ and reviewed the experimental literature. Based on the results presented in that paper we use the following quenching cross sections at 1380 K: $28\pm8$ Å$^2$ for $H_2O$; and $9\pm3$ Å$^2$ for $O_2$. Helium does not appear to quench OH $A\,^2\Sigma^+(\nu'=0)$, and hence, its quenching cross section is taken to be zero. Note that each of these cross sections represents an average quenching cross section for the rotational levels of the $A\,^2\Sigma^+(\nu'=0)$ state. LKK report a decrease in the total measured quenching rate with increasing rotational quantum number. Specifically the total measured quenching rate of the OH $A\,^2\Sigma^+(\nu'=0)$ state increases by approximately 7% from $N'=10$ to $N'=0$. For completeness we take the quenching cross sections for the $F_2(N'=2)$, $F_2(N'=4)$, and $F_2(N'=9)$ levels to be $28\pm8$ Å$^2$, $28\pm8$ Å$^2$, and $27\pm8$ Å$^2$

for $H_2O$; and $9.1\pm3$ Å$^2$, $9\pm3$ Å$^2$, and $8.7\pm3$ Å$^2$ for $O_2$, respectively, which reflect the rotational level dependence of the total quenching rate observed by LKK.

Let us compare the calculated relaxation rates to those measured in the NDFWM experiments. See Table I. The calculated lower limits of the $\Gamma_n(K=0)$ rates for the $^RQ_{21}(1.5)$, $^RQ_{21}(3.5)$, and $^RQ_{21}(8.5)$ transitions are $0.026\pm0.007$ cm$^{-1}$, $0.024\pm0.003$ cm$^{-1}$, and $0.017\pm0.003$ cm$^{-1}$, respectively. Similarly the calculated upper limits of the $\Gamma_n(K=0)$ rates for the $^RQ_{21}(1.5)$, $^RQ_{21}(3.5)$, and $^RQ_{21}(8.5)$ transitions are $0.029\pm0.008$ cm$^{-1}$, $0.028\pm0.004$ cm$^{-1}$, and $0.020\pm0.004$ cm$^{-1}$, respectively. The lower and upper limits of the $\Gamma_n(K=0)$ rates correspond to $R$ and $R+Q+A_{eg}$, respectively. These values agree quite well with the values of Table I considering the approximations made in estimating the state-specific cross sections and the extrapolation to our calculated flame conditions. This level of agreement further supports the fact that the population, the orientation, and the alignment of the total angular momentum distribution relax at different rates, because relaxation rates much faster than the population relaxation rates are necessary to fit the NDFWM line profiles of the $^RQ_{21}(1.5)$ and $^RQ_{21}(3.5)$ transitions. Furthermore we have demonstrated that NDFWM line profiles taken as a function of polarization enable population relaxation rates to be measured directly. This result is significant, because most spectroscopic techniques provide information regarding the dipolar dephasing rate $\Gamma_{eg}$ which contains contributions from pure dephasing (elastic) collisions in addition to energy transfer (inelastic) collisions.

Rea, Chang, and Hanson (RCH)[61] have studied the temperature and rotational quantum number dependence of the broadening of the $A\,^2\Sigma^+-X\,^2\Pi$ (0,0) band of OH in collisions with $H_2O$. The dipolar dephasing rates reported by RCH decrease monotonically with increasing rotational quantum number. This dependence is in qualitative agreement with our results reported in Table I. Dipolar dephasing rates of $0.023\pm0.004$ cm$^{-1}$, $0.022\pm0.003$ cm$^{-1}$, and $0.015\pm0.002$ cm$^{-1}$ for the $^RQ_{21}(1.5)$, $^RQ_{21}(3.5)$, and $^RQ_{21}(8.5)$ transitions, respectively, are calculated using the RCH values and a value of $0.038\pm0.007$ cm$^{-1}$ atm$^{-1}$ for the broadening of the $A\,^2\Sigma^+-X\,^2\Pi$ (0,0) band of OH in collisions with $O_2$.[61,62] These values are approximately a factor of 2 smaller than the results shown in Table I, and adding the small He population relaxation contribution to the dipolar dephasing rates does not make up for the difference. The large differences between the calculated and observed rates suggest that the broadening of the $A\,^2\Sigma^+-X\,^2\Pi$ (0,0) band of OH in pure dephasing (elastic) collisions with He is significant. To our knowledge no collisional broadening coefficients for He are reported, and therefore a direct comparison is not possible. From our data, however, we calculate a value of $0.031\pm0.011$ cm$^{-1}$ atm$^{-1}$ for the broadening of the $A\,^2\Sigma^+-X\,^2\Pi$ (0,0) band of OH in collisions with He.

We have also measured DFWM and NDFWM line profiles of OH in an undiluted $H_2/O_2$ flame with a calculated composition of 89% $H_2O$ and 11% $O_2$ and a measured temperature of $1460\pm80$ K at $5.5\pm0.5$ mm above the burner surface. Unlike the $H_2/O_2$/He flame, thermal grating signal

intensities are large compared to the RFWM response in this flame.[40] We have modeled the NDFWM signal response[63] in the presence of thermal gratings and observed that the ND-FWM line widths of the $^RQ_{21}(1.5)$, $^RQ_{21}(3.5)$, and $^RQ_{21}(8.5)$ transitions do not change significantly as a function of polarization. This insensitivity of the line width to the polarizations of the input fields suggests that the population, the orientation, and the alignment of the total angular momentum distribution relax at nearly the same rate. Because of the additional variables required to fit the NDFWM line shape in the presence of thermal gratings, we are not able to determine a unique set of values for the $K$-dependent relaxation rates. It is possible, however, to obtain approximate values for the dipolar dephasing rates $\Gamma_{eg}$, and these values agree well with the calculated rates. For example we calculate a value for $\Gamma_{eg}$ of $0.082\pm0.012$ cm$^{-1}$ for the $^RQ_{21}(1.5)$ transition which compares well to the experimental value of $0.079 \pm0.018$ cm$^{-1}$. Furthermore, using the relation $\Gamma_{eg}=1/2(\Gamma_g+\Gamma_e)=R+Q/2+A_{eg}/2$ and the population relaxation rates of LKK and Paul, we calculate a value of $0.070\pm0.024$ cm$^{-1}$ for $\Gamma_{eg}$ which suggests that the contribution of pure dephasing (elastic) collisions of OH with $H_2O$ to $\Gamma_{eg}$ is small.[52,64]

## VI. CONCLUSIONS

We have shown that twelve gratings contribute to DFWM and NDFWM signals. The gratings can be distinguished by spacing ($\Delta\mathbf{k}_{12}$ or $\Delta\mathbf{k}_{32}$), by the level in which the grating is formed (ground or excited), and by the multipole nature of the grating (population, orientation, or alignment). We presented data that showed that the DFWM line profile in the limit of large Doppler broadening does not change as a function of the input-field polarizations even when the population, the orientation, and the alignment relax at different rates. The absolute DFWM signal intensity, however, was shown to depend strongly on the values of these relaxation rates. We also showed that these rates can be determined from NDFWM line profiles and that such information is necessary to extract accurate relative internal-state distributions from DFWM signal intensities. The data presented here suggests that the presence of unequal relaxation of the population, the orientation, and the alignment of the total angular momentum distribution is most significant for low values of $J$ for collision partners such as He that favor elastic reorienting collisions over inelastic population transfer collisions. This result is an important finding because the effect of elastic reorienting collisions on the reduction of DFWM spectra to relative populations has hitherto not been considered.

The results presented here may be generalized to any RFWM experiment because in such experiments the signal intensity can always be expressed in the form of Eq. (2) which includes contributions from the $K=0$, 1, and 2 multipole moments of the total angular momentum distribution, i.e., contributions from population, orientation, and alignment gratings (see, for example, Ref. 8). In some RFWM experiments, such as two-color resonant schemes, the number of gratings will be reduced compared to the most general case (12 gratings), but population, orientation, and alignment gratings always contribute to the signal. Therefore the possibility of different relaxation rates for the first three multipole moments of the total angular momentum distribution, i.e., the population, the orientation, and the alignment, must always be considered.

## ACKNOWLEDGMENTS

[1] H. J. Eichler, P. Gunter, and D. W. Pohl, *Laser-Induced Dynamic Gratings* (Springer-Verlag, Berlin, 1986).
[2] S. A. J. Druet and J.-P. E. Taran, Prog. Quantum Electron. **7**, 1 (1981).
[3] M. Ducloy and D. Bloch, Phys. Rev. A **30**, 3107 (1984).
[4] P. R. Berman, D. G. Steel, G. Khitrova, and J. Liu, Phys. Rev. A **38**, 252 (1988).
[5] B. Attal-Trétout, P. Monot, and K. Müller-Dethlefs, Mol. Phys. **73**, 1257 (1991).
[6] S. Williams, R. N. Zare, and L. A. Rahn, J. Chem. Phys. **101**, 1072 (1994).
[7] T. J. Butenhoff and E. A. Rohlfing, J. Chem. Phys. **98**, 5460 (1993).
[8] S. Williams, J. D. Tobiason, J. R. Dunlop, and E. A. Rohling, J. Chem. Phys. **102**, 8342 (1995).
[9] A. B. Myers and R. M. Hochstrasser, IEEE J. Quantum Electron **QE-22**, 1482 (1986).
[10] R. Trebino, E. K. Gustafson, and A. E. Siegman, J. Opt. Soc. Am. B **3**, 1295 (1986).
[11] S. Mukamel, Annu. Rev. Phys. Chem. **41**, 647 (1990).
[12] J. T. Fourkas, R. Trebino, and M. D. Fayer, J. Chem. Phys. **97**, 69 (1992).
[13] J. T. Fourkas, R. Trebino, and M. D. Fayer, J. Chem. Phys. **97**, 78 (1992).
[14] M. Cho, G. R. Fleming, and S. Mukamel, J. Chem. Phys. **98**, 5314 (1993).
[15] T. J. Butenhoff and E. A. Rohlfing, J. Chem. Phys. **98**, 5469 (1993).
[16] D. S. Green, T. G. Owano, S. Williams, D. G. Goodwin, R. N. Zare, and C. H. Kruger, Science **259**, 1726 (1993).
[17] R. L. Farrow and D. J. Rakestraw, Science **257**, 1894 (1992).
[18] T. Dreier and D. J. Rakestraw, Appl. Phys. B **50**, 479 (1990).
[19] B. Yip, P. M. Danehy, and R. K. Hanson, Opt. Lett. **17**, 751 (1992).
[20] P. Ewart and M. Kaczmarek, Appl. Opt. **30**, 3996 (1991).
[21] S. Williams, R. N. Zare, and L. A. Rahn, J. Chem. Phys. **101**, 1093 (1994).
[22] J. Pender and L. Hesslink, Opt. Lett. **10**, 264 (1985).
[23] P. Ewart, P. Snowdon, and I. Magnusson, Opt. Lett. **14**, 563 (1989).
[24] S. Williams, D. S. Green, S. Sethuraman, and R. N. Zare, J. Am. Chem. Soc. **114**, 9122 (1992).
[25] J. T. Fourkas, T. R. Brewer, H. Kim, and M. D. Fayer, J. Chem. Phys. **95**, 5775 (1991).
[26] R. B. Williams, P. Ewart, and A. Dreizler, Opt. Lett. **19**, 1486 (1994).
[27] E. F. McCormack, S. T. Pratt, P. M. Dehmer, and J. L. Dehmer, Chem. Phys. Lett. **227**, 656 (1994).
[28] Q. Zhang, S. A. Kandel, T. A. W. Wasserman, and P. H. Vaccaro, J. Chem. Phys. **96**, 1640 (1992).
[29] T. J. Buttenhoff and E. A. Rohlfing, J. Chem. Phys. **97**, 1595 (1992).
[30] J. F. Lam and R. L. Abrams, Phys. Rev. A **26**, 1539 (1982).
[31] I. Aben, W. Ubachs, G. van der Zwan, and W. Hogervorst, Chem. Phys. **169**, 113 (1993).
[32] E. Freidman-Hill, L. A. Rahn, and R. L. Farrow, J. Chem. Phys. **100**, 4065 (1994).
[33] R. P. Lucht, R. L. Farrow, and D. J. Rakestraw, J. Opt. Soc. Am. B **10**, 1508 (1993).

[34] D. R. Meacher, A. Charlton, P. Ewart, J. Cooper, and G. Alber, Phys. Rev. A **42**, 3018 (1990).

[35] D. R. Meacher, P. G. R. Smith, P. Ewart, and J. Cooper, Phys. Rev. A **46**, 2718 (1992).

[36] P. H. Paul, R. L. Farrow and P. M. Danehy, J. Opt. Soc. Am. B **12**, 384 (1995).

[37] R. L. Farrow, D. J. Rakestraw, and T. Dreier, J. Opt. Soc. Am. B **9**, 1770 (1992).

[38] P. M. Danehy, E. J. Friedman-Hill, R. P. Lucht, and R. L. Farrow, Appl. Phys. B **57**, 243 (1993).

[39] L. A. Rahn and M. S. Brown, Opt. Lett. **19**, 1249 (1994).

[40] S. Williams, L. Rahn, P. H. Paul, J. Forsman, and R. N. Zare, Opt. Lett. **19**, 1681 (1994).

[41] P. M. Danehy, P. H. Paul and R. L. Farrow, J. Opt. Soc. Am. B **12**, 1564 (1995).

[42] K. Blum, *Density Matrix Theory and Applications* (Plenum, New York, 1981).

[43] A. Orr-Ewing and R. N. Zare, in *Chemical Dynamics and Kinetics of Small Radicals*, edited by A. Wagner and K. Liu (World Scientific, Singapore, in press).

[44] T. K. Yee and T. K. Gustafson, Phys. Rev. A **18**, 1597 (1978).

[45] Y. Prior, IEEE J. Quantum Electron. **QE-20**, 37 (1984).

[46] C. H. Greene and R. N. Zare, J. Chem. Phys. **78**, 6741 (1983).

[47] R. N. Zare, *Angular Momentum* (Wiley, New York, 1988).

[48] M. Ducloy and D. Bloch, J. Phys. (Paris) **42**, 711 (1981).

[49] R. L. Abrams, J. F. Lam, R. C. Lind, D. G. Steel, and P. F. Liao, in *Optical Phase Conjugation*, edited by R. A. Fisher (Academic, New York, 1983), Chap. 8.

[50] G. Stark, J. W. Brault, and M. C. Abrams, J. Opt. Soc. Am. B **11**, 3 (1994). G. H. Dieke and H. M. Crosswhite, J. Quant. Spectrosc. Radiat. Transfer **2**, 97 (1962).

[51] A. Goldman and J. R. Gillis, J. Quant. Spectrosc. Radiat. Transfer **25**, 111 (1981); W. L. Dimpfl and J. L. Kinsey, *ibid.* **21**, 233 (1979).

[52] M. S. Brown, L. A. Rahn, and T. Dreier, Opt. Lett. **17**, 76 (1992).

[53] J. E. M. Goldsmith, in *Twentieth Symposium (International) on Combustion* (The Combustion Institute, Pittsburgh, PA, 1984), pp. 1331–1337.

[54] Numerical evaluation of equation of Eq. (2) shows that Eq. (6) is valid for $2\Gamma_{eg}/\Delta\omega_D < 0.1$ and that for $2\Gamma_{eg}/\Delta\omega_D < 0.4$ it is a good approximation.

[55] The homogeneous line broadening parameter obtained from Eq. (6) is 8% smaller than that obtained from Eq. (2).

[56] D. E. Govoni, J. A. Booze, A. Sinha, and F. F. Crim, Chem. Phys. Lett. **216**, 525 (1993).

[57] G. Zizak, G. A. Petrucci, C. L. Stevenson, and J. D. Winefordner, Appl. Opt. **30**, 5270 (1991).

[58] M. P. Lee, R. Kienle, and K. Kohse-Höinghaus, Appl. Phys. B **58**, 447 (1994).

[59] A. Jorg, A. D. Esposti, and H.-J. Werner, J. Chem. Phys. **93**, 8757 (1990); R. Kienle, M. P. Lee and K. Kohse-Höinghaus, Appl. Phys. B (submitted).

[60] P. H. Paul, J. Quant. Spectrosc. Radiat. Transfer **51**, 511 (1994).

[61] E. C. Rea, Jr., A. Y. Chang, and R. K. Hanson, J. Quant. Spectrosc. Radiat. Transfer **41**, 29 (1989).

[62] C. C. Wang, D. K. Killinger, and C.-M. Huang, Phys. Rev. A **22**, 188 (1980).

[63] L. A. Rahn (unpublished results).

[64] R. P. Lucht, D. W. Sweeney, and N. M. Laurendeau, Appl. Opt. **25**, 4086 (1986).